# Multistack Integration of Three-Dimensional Hyperbranched Anatase Titania Architectures for High-Efficiency Dye-Sensitized Solar Cells

Wu-Qiang Wu, Yang-Fan Xu, Hua-Shang Rao, Cheng-Yong Su, and Dai-Bin Kuang*

MOE Key Laboratory of Bioinorganic and Synthetic Chemistry, KLGHEI of Environment and Energy Chemistry, State Key Laboratory of Optoelectronic Materials and Technologies, Lehn Institute of Functional Materials, School of Chemistry and Chemical Engineering, Sun Yat-sen University, Guangzhou 510275, P. R. China

S *Supporting Information*

ABSTRACT: An unprecedented attempt was conducted on suitably functionalized integration of three-dimensional hyperbranched titania architectures for efficient multistack photoanode, constructed via layer-by-layer assembly of hyperbranched hierarchical tree-like titania nanowires (underlayer), branched hierarchical rambutan-like titania hollow submi-crometer-sized spheres (intermediate layer), and hyperbranched hierarchical urchin-like titania micrometer-sized spheres (top layer). Owing to favorable charge-collection, superior light harvesting efficiency and extended electron lifetime, the multilayered TiO_2-based devices showed greater J_{sc} and V_{oc} than those of a conventional TiO_2 nanoparticle (TNP), and an overall power conversion efficiency of 11.01% (J_{sc} = 18.53 mA cm^{-2}; V_{oc} = 827 mV and FF = 0.72) was attained, which remarkably outperformed that of a TNP-based reference cell (η = 7.62%) with a similar film thickness. Meanwhile, the facile and operable film-fabricating technique (hydrothermal and drop-casting) provides a promising scheme and great simplicity for high performance/cost ratio photovoltaic device processability in a sustainable way.
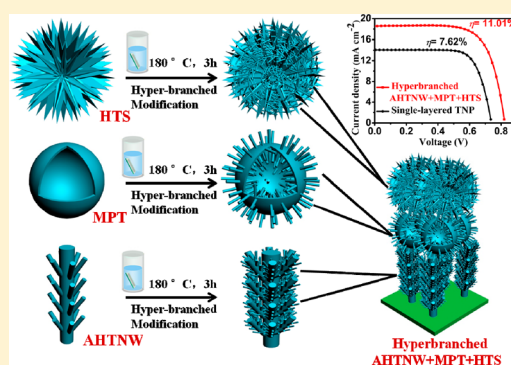
1. INTRODUCTION

In modern-day society, the stringent global energy demand, excessive exhaustion of fossil fuels and overwhelming environmental pollution have called for the development of new types of renewable, sustainable, and clean energy-related devices with a high performance/cost ratio.[1−4] Of particular interest are the photovoltaic technologies for affordable and widespread solar-to-electricity processes used in the household and industry domains. Among various photovoltaic devices, dye-sensitized solar cells (DSSCs) as the third-generation representatives, to date have already exhibited a certified high record power conversion efficiency of 12.3% via exploitation of a 20 nm anatase TiO_2 nanocrystalline photoanode sensitized by zinc porphyrin dye.[5]

It is widely known that TiO_2 film is one of the most effective oxide photoanodes in DSSCs.[6−8] An ideal TiO_2 film should simultaneously satisfy several major factors, such as a large specific surface area for sufficient dye uptakes; a superior scattering effect for enhanced light-harvesting; a prominent electron transport and recombination characteristic for efficient charge-collection; and an adequate network and porosity for feasible electrolyte penetration.[9−13] However, more often than not, these factors are mutually incompatible to each other.[14−17] For a state-of-the-art highly efficient DSSC, TiO_2 film with hierarchical structures consisting of nanoparticles (i.e., meso-porous spherical beads, mesospheres, etc.)[18−20] exhibited an excellent bifunctional character (dye-loading ability and light-scattering effect). But there is one fatal problem existing in such

nanostructures: the diffusion of electrons will be restricted by trapping/detrapping events along numerous defects and grain boundaries which are present in the disordered interstices of TiO_2 nanoparticle building blocks, thus leading to unsatisfied electron lifetime (lower photovoltage, <800 mV). One remedy for this problem is to introduce branched hierarchical TiO_2 nanoarchitectures consisting of various competitive 1D nanostructure building blocks, such as nanorods,[21] nano-spindles,[22] and nanotubes,[23] to facilitate electron transport for enhanced charge-collection efficiency and thus prolong electron lifetime. The all-linear 1D nanostructure building blocks confer an advantage of rapid unidirectional electron percolation for rapid collection of photogenerated electrons. Nevertheless, most of such branched TiO_2 hierarchical nanostructures do not possess as large internal surface area as conventional 20 nm nanoparticle counterparts. Hence, there is still plenty of research to be done on the design and synthesis of hyperbranched materials, which should further enlarge the surface area to attain dye loading to a sufficient extent.

Another versatile strategy to fabricate an efficient photo-anode is to optimize film composition. For instance, a single TiO_2 layer contains small-sized nanocrystallines and large-sized light scatters (submicrometer beads, microspheres, spherical voids, etc.)[24,25] or the TiO_2 films feature a double-layered structure comprising a 2−5 μm hazy scattering top layer and a

12–14 μm transparent nanocrystalline underlayer.[26–28] These structures are believed to ensure an acceptable value of the effective surface area for optimal dye adsorption and enhance the light-harvesting efficiency over a broad wavelength range. Recently, multilayered structures assembled by tailoring stacks of purposely selected TiO$_2$ with various shapes and sizes have been reported for DSSC application.[29–32] The multilayer is considered to be a promising configuration with complementary and synergistic properties in which multifunctionalities of TiO$_2$ such as sufficient dye-loading, high light-harvesting efficiency, and superior electron transport can be fulfilled simultaneously.

In this article, we present an operable and versatile approach to fabricate an engineered multistack photoanode by suitably incorporating branched TiO$_2$ architectures with tunable functionality. The significance of the present work is emphasized on a pioneer large-scale TiO$_2$ film-making with a multistack configuration design of anatase hierarchical TiO$_2$ nanowires (AHTNW, underlayer), submicrometer macroporous TiO$_2$ hollow spheres (MPT, intermediate layer), and hierarchical TiO$_2$ microspheres (HTS, top layer) on a fluorine doped tin oxide (FTO) glass substrate. Most importantly, greater attention has been paid to the subsequent facile hydrothermal treatment of such a multilayered photoanode to grow additional anatase short TiO$_2$ nanorod branches on each TiO$_2$ layer in the presence of titanium potassium oxalate, water, and diethylene glycol. This approach improves the design of the multilayered photoanodes consisting of layer-by-layer distinct hyperbranched TiO$_2$ architectures, namely, hyperbranched hierarchical tree-like titania nanowires, hyperbranched hierarchical rambutan-like titania hollow submicrometer spheres, and hyperbranched hierarchical urchin-like titania microspheres. These multistack devices showed significantly greater J_{sc} and V_{oc} than those of the NP reference counterparts, attaining an elevated milestone efficiency of 11.01% at total film thickness of 34 μm. The present approach opens up a low-cost facile operation route with great simplicity for fabricating an effective and efficient photoanode that simultaneously accommodates high specific surface area, fast electron transport, efficient charge collection, and pronounced light harvesting.

2. EXPERIMENTAL SECTION

2.1. Synthesis of a Multilayered AHTNW–MPT–HTS–Branched Photoanode. First, a K$_2$TiO(C$_2$O$_4$)$_2$/deionized water/diethylene glycol mixture solution was transferred into Teflon-liner. Then a TiO$_2$-coated, FTO glass substrate (100 nm thick TiO$_2$ seed layer) was placed at an angle against the wall of the Teflon-liner with the conducting side facing down, and a Teflon-lined stainless steel autoclave was performed at 180 °C for 9 h for the growth of vertically aligned AHTNW on FTO glass.[33] Second, for the template-assisted synthesis of MPT, 0.4 mL of butyl titanate was mixed with 20 mL of ethanol under vigorous stirring at 70 °C for 2 h followed by addition of 4 mL of PS aqueous solution and kept stirring for another 12 h. The as-obtained TiO$_2$ nanoparticle-covered polystyrene (PS) spheres solution was then rinsed with ethanol and distilled water, and then uniformly dispersed in ethanol under an ultrasonic bath. Afterward, the TiO$_2$ nanoparticle-covered PS spheres ethanol solution was dripped by a pipet onto the surface of the AHTNW/FTO substrates. The substrates were then calcined in a box furnace at 500 °C for 1 h to remove the PS templates and to form the double-layered AHTNW +MPT/FTO photoanode. Third, HTS was hydrothermally synthesized according to our previous report, which is in a butyl titanate/acetic acid sol system.[21] The collected sample powders were also dispersed in ethanol and then dripped onto the surface of the AHTNW+MPT/FTO photoanode to form the trilayered AHTNW +MPT+HTS/FTO photoanode. Last but not least, the as-prepared trilayered photoanode underwent another facile hydrothermal process in a mixture solution of 0.35g of K$_2$TiO(C$_2$O$_4$)$_2$, 17.5 mL of diethylene glycol (DEG), and 2.5 mL of deionized water at 180 °C for 3 h, in order to form a multilayered AHTNW+MPT+HTS–branches/FTO photoanode consisting of hyperbranched hierarchical TiO$_2$ architectures. The size of the obtained films was approximately 2 cm × 3 cm (Supporting Information, Figure S1e), and the films remained smooth and intact without any rupture or bubble during the overall fabrication process.

2.2. Morphology Characterization. The morphological structure of the TiO$_2$ samples was observed with the field emission scanning electron microscopy (FE-SEM, JSM-6330F) and high-resolution transmission electron microscope (FE-HRTEM, JEOL-2010 HR). The crystal phases of the products was examined by X-ray diffraction (XRD, Bruker D8 Advance) in a 2θ range from 10° to 80°.

2.3. DSSCs Fabrication. The as-prepared AHTNW, AHTNW +MPT, AHTNW+MPT+HTS, and AHTNW+MPT+HTS-branches on FTO glass with required film thickness (active size is 0.16 cm^2) were applied as photoelectrodes for dye-sensitized solar cells. For comparison, a 34 μm thick anatase TNP-based photoanode was prepared via a screen-printing method and then used to fabricate solar cells as well. The as-prepared TiO$_2$ photoanode was immersed into a TiCl$_4$ fresh aqueous solution (40 mM) at 70 °C for 30 min and washed with water and ethanol, then sintered at 520 °C for 30 min. The TiO$_2$ electrodes were sensitized in a solution (0.5 mM N719 dye in acetonitrile/*tert*-butanol (v/v = 1:1) for 16 h. The preparation of I^-/I_3^- redox electrolyte was similar to our previous report.[34] The electrolyte solution was introduced into the space between the photoanodes and Pt-sheet counter electrode.

2.4. Photovoltaic and Photoelectric Characterization. The photocurrent density-photovoltage (J–V) characteristics were measured by a Keithley 2400 source meter under simulated AM 1.5 G illumination (100 mW cm^{-2}) provided by a solar light simulator (Oriel, model: 91192), calibrated with a standard Si solar cell. To make the efficiencies measurement more reliable, at least six identical cells based on each sample were assembled and characterized. The average standard deviation was ± 0.2%. The IPCE spectra as a function of wavelength from 400 nm to 800 nm was measured with a Spectral Products DK240 monochromator. The diffuse reflectance spectra of TiO$_2$ film were measured on a UV–vis–NIR spectrophotometer (UV-3150) to evaluate their reflectance performance. For the evaluation of dye-loading amount of TiO$_2$ films, the absorption spectra of N719 dye-desorption solutions from the TiO$_2$ films (dye-absorbed TiO$_2$ film was immersed into 0.1 M NaOH aqueous solution) on a UV–vis–NIR spectrophotometer (UV-3150). Electrochemical impedance spectroscopy (EIS) was performed with a Zennium electrochemical workstation (ZAHNER) in a frequency range between 10 mHz and 1 MHz. The magnitude of the alternative signal was 10 mV. The impedance measurements were carried out under a forward bias of −0.80 V in the dark condition. The resulting impedance spectra were fitted with Z-view software. The intensity-modulated photocurrent/photovoltage spectroscopy (IMPS/IMVS) measurements were conducted on a electrochemical workstation (Zahner, Zennium) with a frequency response analyzer under modulated green light emitting diodes (457 nm) driven by a source supply (Zahner, PP211), which can provide both dc and ac components of the illumination. The frequency range was set from 100 kHz to 0.1 Hz. The incident light intensity was controlled from 30 to 150 mW cm^{-2}.
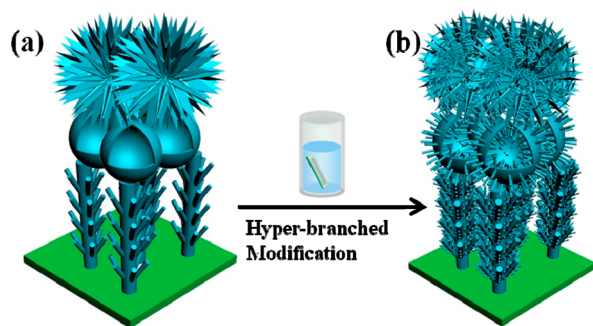
3. RESULTS AND DISCUSSION

3.1. Fabrication Technique of Multistack TiO$_2$ Photoelectrode with Hyperbranched Architectures. The schematic diagram of the fabrication process of layer-by-layer multistack junctions of TiO$_2$ photoanodes and various authentic resultant TiO$_2$ films with large-scale area are demonstrated in the Supporting Information, Figure S1. Briefly, in the first step, AHTNW-grown FTO glass served as a substrate for the subsequent attachment of other TiO$_2$ layers

(Supporting Information, Figure S1a). Typically, the synthesis of AHTNW involved a simple surfactant-free hydrothermal process[33] using titanium potassium oxalate as a precursor in a mixture solution containing deionized water and diethylene glycol. Afterward, submicrometer-sized MPT with hollow structure and micrometer-sized HTS[21] were successively dripped onto the top of the prior TiO_2 film. Consequently, the MPT layer and HTS layer hold their place as second and third layer, respectively, to construct the FTO−AHTNW−MPT (Supporting Information, Figure S1b) and FTO−AHTNW−MPT−HTS (Figure S1c) multistack junction configuration. Finally, the as-prepared three-layer stack photoanode experienced another facile hydrothermal treatment for the anisotropic growth of the short TiO_2 nanorod branches on each layer of the TiO_2 structures. Interestingly enough, a three-layer stack of photanode, namely, FTO−AHTNW−MPT−HTS−branches (Supporting Information, Figure S1d), consisting of hyperbranched TiO_2 architectures was unprecedentedly obtained. Herein, Scheme 1 unambiguously depicts the sketch

Scheme 1. Schematic Sketch for the Hyperbranched Modification of Multilayered TiO_2 Photoanode on FTO Glass[a]


[a](a) Parental three-layer TiO_2 photoanodes consisting of AHTNW bottom layer, MPT intermediate layer, and HTS top layer; (b) corresponding three-layer TiO_2 photoanodes consisting of hyperbranched TiO_2 architectures.

of hyperbranched modification of the parental FTO−AHTNW−MPT−HTS trilayered architectures, which leads to much more complicated and interconnected FTO−AHTNW−MPT−HTS−branches architectures.

3.2. Morphological Structure of Multistack TiO_2 Photoelectrode with Hyperbranched Architectures. Figure 1 shows SEM images of the three-layer stack TiO_2 photoanode and highlights the unique hyperbranched morphologies of individual titania nano/microstructure. Obviously, a high-quality three-layer stack of TiO_2 photoanodes consisting of 18 μm thick hyperbranched hierarchical titania nanowires (underlayer), 8 μm thick branched hierarchical titania hollow submicrometer-sized spheres (intermediate layer) and 8 μm thick hyperbranched hierarchical titania micrometer-sized spheres (top layer) was unambiguously observed (Figure 1a). Interestingly, the intact geometric features of TiO_2 architectures were safely preserved even after the calcination and hydrothermal treatment; for instance, the TiO_2 with hierarchical structures did not collapse into segregated agglomerates and/or generate numerous cracks. In addition, the XRD patterns (Supporting Information, Figure S2) confirmed the purely anatase TiO_2 crystal structure of such a film, without any detectable secondary phases, for which two
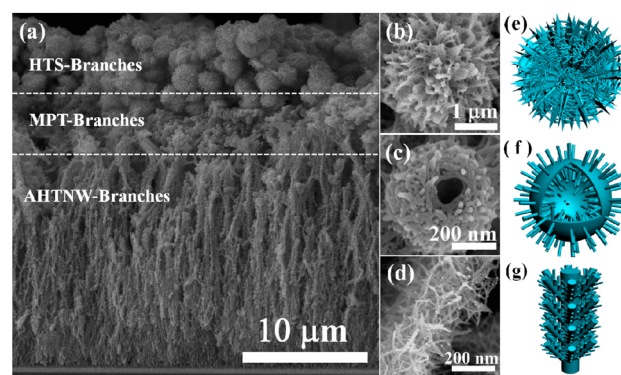

Figure 1. (a) Cross-sectional SEM image view of three-layer stacking of TiO_2 photoanodes. SEM images and corresponding schematic sketches of the each layer of TiO_2 nano/microstructures: (b, e) HTS branches; (c, f) MPT branches; (d, g) AHTNW branches.

characteristic diffraction signals of the (101) and (200) facets were unambiguously observed.

Such a multilayered TiO_2 photoanode comprising various hyperbranched TiO_2 architectures was constructed from a layer-by-layer procedure followed by a facile hydrothermal growth of secondary TiO_2 short nanorods branches with tiny diameters. The cross-sectional SEM images of single-layered AHTNW (18 μm in thickness), double-layered AHTNW+MPT (26 μm in thickness), and trilayered AHTNW+MPT+HTS (34 μm in thickness) as well as single-layered TNP (34 μm in thickness) were showcased in Supporting Information, Figure S3. Also, the surface SEM images showing the uniform distribution of the second MPT layer and the third HTS layer can be seen in Figure S4, which validates the feasibility and effectiveness of our proposed layer-by-layer assembly of multistack architecture via a simple drop-casting procedure. In particular, for the FTO−AHTNW−MPT−HTS junction, one can notice the well-connected attachment between the HTS−MPT interface and AHTNW−MPT interface (Supporting Information, Figure S5), which confirms that the interfaces between each layer assembly are close and thus beneficial to transport photogenerated electrons efficiently from layer to layer. Moreover, the magnified SEM images showing individual hyperbranched TiO_2 architecture were seen in Figure 1 panels, b (HTS branches), c (MPT branches), and d (AHTNW branches), and the high-likeness sketches were accordingly displayed in Figure 1 panels e, f, and g, respectively.

Since the hyperbranched modification of engineered multistack TiO_2 photoanodes that we achieved in the present work has never been reported elsewhere, it is of great necessity to uncover the intrinsic aspects of such a TiO_2 hyperbranched architecture. The detailed morphologies of AHTNW, MPT, HTS, and their corresponding hyperbranched derivants were visible in the SEM images of Figure 2, and the fine structure of hyperbranched architectures were displayed in TEM images of Figure 3.
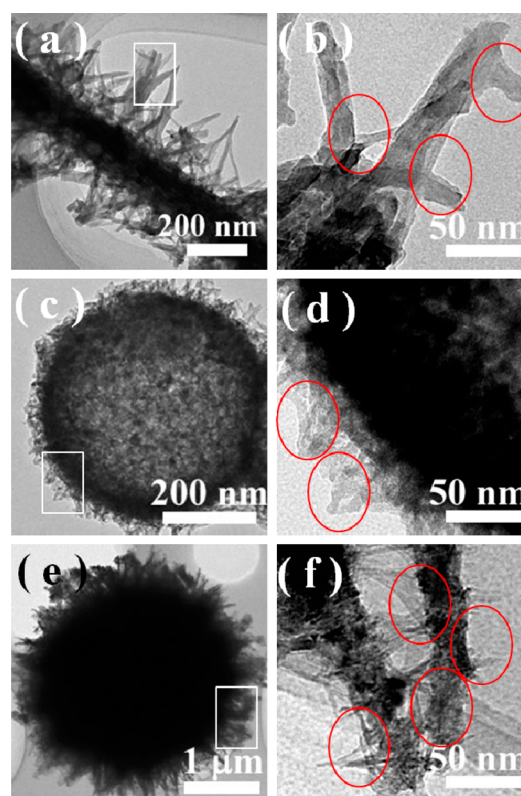
Specifically, AHTNW was consisting of long TiO_2 nanowires trunks (250 nm in diameter) and numerous short nanorods branches (50−60 nm in diameter, 50−150 nm in length) (Figure 2a,b). After the hyperbranched modification, some secondary tiny TiO_2 nanobranches (10−20 nm in diameter and length) were grown on the original nanorods to form the arborisation-like structures (seen in Figure 2c,d and Figure 3b). Similarly, slender TiO_2 nanobranches with higher aspect-ratio (3−5 nm in diameter and 20−40 nm in length) were
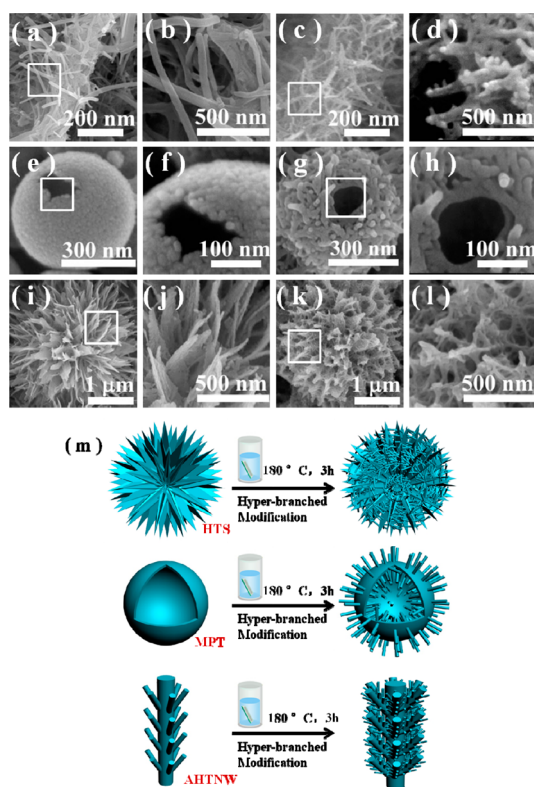
Figure 2. SEM and corresponding magnified images of the as-prepared (a, b) AHTNW, (e, f) MPT, and (i, j) HTS and their respective hyperbranched derivants: (c, d) AHTNW branches, (g, h) MPT branches, and (k, l) HTS branches. (m) A schematic illustration of hyperbranched modification of parental HTS, MPT, and AHTNW to form HTS branches, MPT branches and AHTNW branches.

Figure 3. TEM and HRTEM images of three families of hyperbranched TiO_2 nano/microstructures: (a, b) AHTNW branches; (c, d) MPT branches; (e, f) HTS branches.

intelligently germinated on the primary nanorod building blocks of the HTS (~3 μm in diameter) (Figure 3f and Figure 2 panels i–l). In terms of MPT parental backbones, subsequent hydrothermal growth leads to the formation of branched hollow spheres, in which numerous nanorods (10–15 nm in diameter and 20–30 nm in length) uniformly covered the surface of MPT with anisotropically oriented linear (Figure 3d and Figure 2 panels e–h) and exhibited interconnected and interlocking features. Consistent with the above SEM images observations, the TEM images of the AHTNW branches, MPT branches and HTS branches in Figure 3a, 3c, and 3e exhibited mainly entire morphologies of three different TiO_2 components, and the hyperbranched shapes are highlighted with red circles shown in Figure 3 panels b, d, and f.

3.3. Photovoltaic Performance, Optical Properties, and Charge Transfer Dynamics. Observations on previously reported prominent photovoltaic properties of individual AHTNW, MPT, as well as HTS (i.e., fast electron transport, preferred reduced recombination, and stronger light scattering effect)[21,33] suggested that we exploit the potential of the complementary and synergistic effects of a suitable combination of these morphologies in a multilayered stack architecture. Such an integrated structure is thought to be more efficient than the monolayer counterparts for many applications. We thus utilized the entire three families of the synthesized TiO_2 architectures to design and fabricate an engineered photoanode within a unique multistack integration in such a way for DSSC application, to simultaneously combine the desirable properties associated with their respective features.

The devices were fabricated with various TiO_2 photoanode configurations, N719 dye, iodide/triiodide electrolyte, and Pt sheet counter electrode. In all cases, the thickness of the AHTNW layer was fixed at ~18 μm, which is in good agreement with our previous work.[33] In the current work, vertically grown AHTNW nanoarrays on a FTO glass substrate were the powerful transfer media that guaranteed efficient electron extraction from the oxide materials to the FTO glass and thus ensure rapid collection of carriers generated throughout the devices because of the exceptional 1D fast and direct electron transfer pathway. Then the deposition of other TiO_2 layers, with relatively larger sizes, such as the successive submicrometer-sized MPT and the micrometer-sized HTS layer on the top of AHTNW, revealed to be the most suitable photon-recycling, light-recapturing structure for efficient and effective light-harvesting. We thus fabricated the structure of double-layered FTO−AHTNW−MPT and trilayered FTO−AHTNW−MPT−HTS photoanode-based DSSCs. First, we tested the effect of the film thickness of the MPT layer and HTS layer on device performance. Specifically, the thickness of the MPT layer and HTS layer was easily controllable across a broad range from 4 to 12 μm with the aim to optimize the balance among the specific characteristics of the added TiO_2 architectures. One can notice that a film thickness of 8 μm is optimal for the MPT intermediate layer and HTS top layer (the corresponding photovoltaic parameters are summarized in Supporting Information, Table S1). Then the optimized trilayered AHTNW−MPT−HTS photoanode underwent further hydrothermal treatment to form AHTNW−MPT−HTS hyperbranched architecture, denoted as AHTNW−MPT−HTS−branches. Figure 4 shows the photo-

6440

dx.doi.org/10.1021/ja5015635 | *J. Am. Chem. Soc.* 2014, 136, 6437−6445
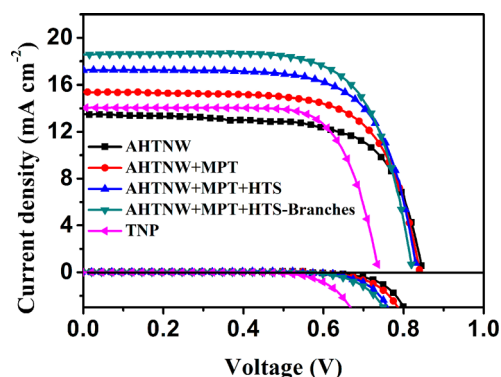
Figure 4. $J-V$ curves of DSSCs fabricated using the different TiO_2 photoanodes under one sun AM 1.5 G illumination (100 mW cm^{-2}) and in the dark condition.

current density–voltage ($J-V$) characteristics of DSSCs fabricated using various structures of TiO_2 photoanodes under a AM 1.5G solar light illumination (100 mW cm^{-2}). As a reference for comparison, anatase TNP-based films with similar thickness were also assembled into DSSCs and tested. The photovoltaic characterization results of five devices are summarized in Table 1. The performances of these devices

Table 1. Summary of Device Parameters Obtained from DSSCs Employing Various TiO_2 Photoanodes with Different Film Thickness under One Sun Illumination (AM 1.5G, 100 mW cm^{-2})

DSSCs	J_{sc}/mA cm^{-2}	V_{oc}/mV	η/%	FF	adsorbed dye/nmol cm^{-2}
AHTNW	13.51	848	7.83	0.68	108.5
AHTNW +MPT	15.37	841	8.96	0.69	140.7
AHTNW +MPT+HTS	17.26	833	10.06	0.70	200.3
AHTNW +MPT +HTS- branches	18.53	827	11.01	0.72	251.4
TNP	14.06	738	7.62	0.73	338.6

exhibited an increasing order of J_{sc} from monolayer AHTNW (13.51 mA cm^{-2}) to trilayered AHTNW−MPT−HTS (17.26 mA cm^{-2}) along with continuously added layer and increased film thickness, but the V_{oc} showed an opposite trend in that V_{oc} was suppressed from 848 mV (AHTNW) to 833 mV (AHTNW−MPT−HTS), indicating the charge recombination is more serious in a thicker film. As for the AHTNW−MPT−HTS−branches based devices, even though V_{oc} experienced a further decline to 827 mV, the overall performance of such devices was primarily dominated by significantly enhanced J_{sc} owing to the enlarged dye-loading capability and boosted light-scattering effects, allowing the surprisingly high efficiency of 11.01% under an optimized hyperbranched condition. The systematic variation of J_{sc} is consistent with the dye uptakes amount on the TiO_2 films, for which the dye loading amount of AHTNW−MPT−HTS−branches (251.4 nmol cm^{-2}) is tremendously higher than that of the monolayer AHTNW one (108.5 nmol cm^{-2}). Because of the countertendency between J_{sc} and V_{oc}, the DSSC−AHTNW−MPT−HTS− branches with a maximum efficiency were distinguished by a J_{sc} of 18.53 mA cm^{-2} and a V_{oc} of 827 mV, while a reference TNP based DSSC with the same thickness (34 μm) gave an

efficiency of only 7.62% with a J_{sc} of 14.06 mA cm^{-2} and a V_{oc} of 738 mV. Despite that the dye-loading amount values are much greater for TNP than for AHTNW−MPT−HTS− branches at a similar thickness because of much smaller particle size (20 nm) for the former, the 34 μm thick TNP film could hardly increase photon harvest, and such a thick TNP would probably provide additional trapping sites for charge recombination.[35] In contrast, the best performance of the hyper-branched multistack photoanode-based devices occurred at an overall film thickness of 34 (18 + 8 + 8) μm. This illustrates the fact that our design for such a hyperbranched multistack TiO_2 photoanode with robust and remarkable mechanical strength is feasible, and in that manner, is verified to overcome the shortage of comparatively small specific surface area while advantageously improving the light-harvesting efficiency, diminishing the possibility of charge recombination as well as facilitating charge-collection efficiency, and thus allowing observed appreciable J_{sc} and V_{oc}. Furthermore, when compared to TNP counterpart-based devices with an optimized film thickness (15−16 μm), the photovoltaic performance (J_{sc} = 18.57 mA cm^{-2}, V_{oc} = 827 mV, η = 11.01% and FF = 0.72) for the 34 μm branched multistack TiO_2 photoanode is also much superior than that of the 15 μm anatase nanoparticle counterpart (J_{sc} = 15.06 mA cm^{-2}, V_{oc} = 806 mV, η = 8.39% and FF = 0.69) (seen in Supporting Information, Table S2). Further details about the reproducibility of DSSC with best performance are listed in the Supporting Information (Table S3), which further validates that the representative maximum photovoltaic results showcased in Table 1 obtained from the $J-V$ measurements are reliable. Moreover, we found a systematic trend for the dark current of the five devices, which decreased linearly with the order of P25 > AHTNW−MPT−HTS− branches > AHTNW−MPT−HTS > AHTNW-MPT > AHTNW. The higher the dark current, the more serious charge recombination and thus the lower the V_{oc} can be achieved. This result is in parallel with the reversed variation trend of V_{oc}. Also, to examine the inherent photovoltaic performance of each layer of TiO_2 architecture, we accordingly fabricated DSSCs using 18 μm AHTNW, 8 μm MPT and 8 μm HTS photoanode as well as their corresponding hyperbranched architectures, and the results are summarized in Table S4. These pieces of evidence corroborated the fact that the hyperbranched transformation of the films did make a favorable impact on their eventual photovoltaic performances.

Given the fact that our priority is to equitably elaborate the intrinsic advantages of the as-prepared three-layered photoanode comprising of hyperbranched TiO_2 architectures, we choose three representative photoanode structures with the same film thickness (34 μm), namely, AHTNW−MPT−HTS, AHTNW−MPT−HTS−branches, and TNP. Figure 5a shows the incident photon-to-current conversion efficiency (IPCE) spectra obtained from the aforementioned representative structures. Clearly, the multilayered configuration, be it AHTNW−MPT−HTS or AHTNW−MPT−HTS−branches, shows an impressive response and thus markedly higher IPCE values than that of the TNP cell over the whole spectral range from 380 to 800 nm. This could be due to the enhanced light scattering and efficient charge collection within multi-layered TiO_2 photoanode based devices compared with TNP counterparts. In the wavelength range between 450 and 650 nm corresponding to the region of N719 maximum absorption, the topmost IPCE values occurred at the AHTNW−MPT−HTS− branches based cell, resulting in the highest J_{sc} of 18.53 mA
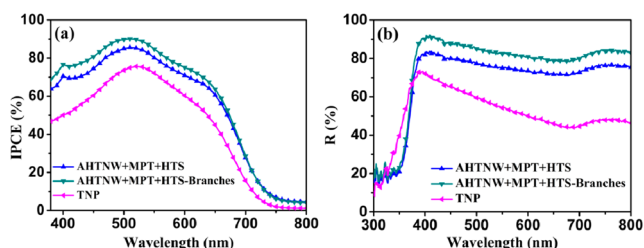
Figure 5. (a) IPCE spectra and (b) Diffuse reflectance spectra of DSSCs fabricated using AHTNW+MPT+HTS, AHTNW+MPT+HTS-branches and TNP photoanode with the same film thickness (34 μm).

cm^{-2}. When the IPCE spectra based on AHTNW−MPT−HTS and AHTNW−MPT−HTS−branches were elaborately compared, one interesting phenomena merits attention. A shifted upward trend was observed on the AHTNW−MPT−HTS−branches based cell with respect to the AHTNW−MPT−HTS one. This improvement, exhibited over a wide range from 380 to 650 nm, could be partially attributed to the scattering effect of the additional short TiO$_2$ nanorods branches, but rather it should also be ascribed to the enhanced optical absorption brought about by extended dye-loading capability owing to such hyperbranched network modification.

The optical properties of these different types of TiO$_2$ films photoanodes were characterized in terms of diffused reflectance spectra. First of all, enhanced reflectance was shown in the order of AHTNW < AHTNW-MPT < AHTNW−MPT−HTS < AHTNW−MPT−HTS−branches (Figure S6), indicating higher light-scattering effect for thicker films. As expected, it can be seen in Figure 5b that both the AHTNW−MPT−HTS and AHTNW−MPT−HTS−branches based film exhibited dramatically higher diffuse reflectance over a broad wavelength range with respect to TNP film. And the AHTNW−MPT−HTS−branches-based film showed the highest reflectance among the three types of films, for which the aggregate size and dimension of such multilayered configuration with complicated and interconnected network of hyperbranched architectures dominates the most significant enhancement of the light-scattering effect within the cells, and this is also a crucial contribution to the boosting of elevated J_{sc} and thus η.

On the other hand, to highlight the effects and advantages of the multistack TiO$_2$ photoanode fabricated via the subsequent drop-casting procedure and hydrothermal treatment, the detailed comparison of relevant photovoltaic performance between original AHTNW and the final AHTNW−MPT−HTS−branches products-based devices merits attention. On balance, after the multistack integration and subsequent hyperbranched modification, a significant increase for dye loading amount up to 130% (251.4 nmol cm^{-2} vs 108.5 nmol cm^{-2}, seen in Table 1) and enhancement for reflectance ability up to 30% (seen in Supporting Information, Figure S6) have been witnessed for AHTNW−MPT−HTS−branches, despite of the fact that the charge recombination within such multistack photoanodes is more serious than that of the pristine AHTNW one owing to the enlarged surface area and much more complicated architectures that would bring about unexpected defects and trapping sites for recombination (dark current analysis in Figure 4). Eventually, a markedly enhanced efficiency over 11% was achieved for AHTNW−MPT−HTS−branches-based cells owing to the significantly enlarged surface area for anchoring many more dye molecules and enhanced

light-scattering ability for prominent light harvesting efficiency, which is much higher than that of pristine AHTNW-based devices (7.83%).

Electrochemical impedance spectroscopy (EIS) is a powerful characterization technique to give an elucidative insight into electrochemical behavior within DSSCs. Figure 6a shows the
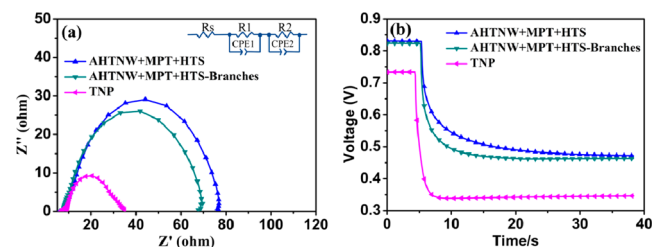

Figure 6. (a) Electrochemical impedance spectra and (b) open-circuit voltage decay curves of DSSCs fabricated using AHTNW+MPT+HTS, AHTNW+MPT+HTS-branches and TNP photoanode with the same film thickness (34 μm). The inset in panel a is the equivalent circuit applied to fit the resistance data.

Nyquist plots of EIS for the DSSCs based on three different TiO$_2$ structures. The corresponding equivalent circuit is shown in the inset and the estimated resistance parameters are listed in Supporting Information, Table S5. In all the EIS Nyquist spectra, two well-defined semicircles can be observed in the high frequency region (>1 kHz) and medium frequency region (1−100 Hz), which represent the charge transfer at the interface of counter electrode/electrolyte (small semicircle) and TiO$_2$/dye/electrolyte (large semicircle), respectively.[36] The electron lifetime (τ_r) values of photoelectrons in a photoanode can be calculated according to the equation $\tau_r = R_2 \times CPE2$, where R_2 represents the recombination resistance and CPE2 represents chemical capacitance.[37] Specifically, the discrepancy showcased in the large semicircles reflects that there is a huge difference lying in the recombination process within different DSSCs. As shown in Supporting Information, Table S5, the R_2 of AHTNW−MPT−HTS, AHTNW−MPT−HTS−branches, and TNP-based DSSCs was 70.0, 63.4, and 23.9 Ω, respectively, and the corresponding τ_r was 113, 88, and 54 ms, respectively. It is worth noting that our engineered multistack integration of the TiO$_2$ photoanode were characterized by a considerably slower charge recombination rate within the DSSCs with respect to reference TNP film based devices which is believed to possess numerous defects, surface states, and grain boundaries throughout their randomly oriented network.[38,39] The fact also confirmed the superior property of effectively suppressing the photogenerated electrons from recombining with oxidizing species, such as I$_3^-$ in the redox electrolyte, resulting favorably in higher charge collection efficiency, longer electron lifetime, and thus increment of J_{sc} and V_{oc} for such a multilayered TiO$_2$ photoanode. Under the open-circuit conditions, the recombination kinetics could also be investigated by the evaluation of the photovoltage decay rate, which is proportional to the rate of charge recombination.[40] Figure 6b shows the plots of V_{oc} decay rate as a function of time within the DSSCs based on the aforementioned three types of TiO$_2$ photoanodes. It is evident that DSSCs based on AHTNW−MPT−HTS and AHTNW−MPT−HTS−branches exhibited a smaller rate of photovoltage decay than that of the TNP-based device, leading to slower recombination kinetics, and thus a longer electron lifetime was achieved. Alternately the TNP-

based cells experienced the fastest voltage decay rate among the three DSSCs, indicating the fastest recombination rate within such cells. As a consequence, the serious reduction of V_{oc} to a comparatively lowest level of 738 mV for TNP cell has been witnessed when the film thickness was up to 34 μm. This result is in concurrence with the observed dark current and EIS studies shown above.

3.4. Electron Transport and Diffusion, Charge Recombination, and Charge-Collection Characteristics.

Intensity-modulated photocurrent spectroscopy (IMPS) and intensity-modulated photovoltage spectroscopy (IMVS) have been performed to further provide quantitative information on electron transport and recombination of DSSCs based on the three different TiO$_2$ films. Briefly, the transport time (τ_d) and electron lifetime (τ_r) can be derived from the IMPS and IMVS measurements according to the equations: $\tau_d = 1/2\pi f_d$ and $\tau_r = 1/2\pi f_r$, respectively, where f_d and f_r are the characteristic minimum frequency of the IMPS and IMVS imaginary component.[41] For the kinetics of electron transport and charge recombination of the devices, τ_d and τ_r represent the time constant of injected electrons transport through the photoanode films and recombination with I$_3^-$ in the electrolyte, respectively. We herein shows the transport time and lifetime of the DSSCs based on the above three TiO$_2$ photoelectrodes as a function of various light intensity (30−150 mW cm^{-2}) in Figure 7a. Our results indicate that τ_d values of AHTNW−
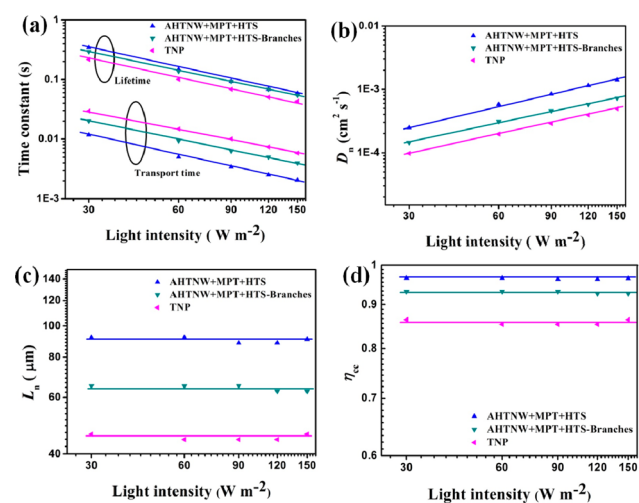
Figure 7. (a) Electron transport time and electron lifetime; (b) electron diffusion coefficient (D_n); (c) effective diffusion length (L_n); (d) charge-collection efficiency (η_{cc}) as a function of light intensities for the DSSCs based on AHTNW+MPT+HTS, AHTNW+MPT+HTS-branches, and the TNP photoanode.

MPT−HTS and AHTNW−MPT−HTS−branches-based DSSC are much smaller than that of TNP-based cell when compared at the same light intensity level, implying that electrons inside multilayered TiO$_2$ architectures transported more rapidly than those inside the TNP electrode, for which shorter durations of transport are required for such cells to collect the electrons at the TCO electrode. Moreover, the longer τ_d for the hyperbranched multilayered architectures compared with those of the the parental one may stem from an elongated electric pathway brought about by additional growth of short TiO$_2$ nanorods branches. On the other hand, one can notice that τ_r values of the AHTNW−MPT−HTS and AHTNW−MPT−HTS−branches-based cells are similar but

much larger than that of the TNP-based device compared at the same light intensity, indicating that the charge recombination is relatively more suppressed at the multilayered photoelectrode/electrolyte interface, which is consistent with a significant discrepancy of V_{oc} showing an average ~85 mV advance for the multilayered photoanode-based devices over the TNP counterpart (Table 1). Relative to that of AHTNW−MPT−HTS, its hyperbranched counterpart exhibited a slightly inferior electron lifetime due to the enlarged surface area which provides more surface trapping sites for mediating recombination with I$_3^-$ in the electrolyte, resulting in a decreased V_{oc}. It is presumed that the robust mechanical connection of each TiO$_2$ layer and well interconnected networks of primary building blocks with multilevel hierarchy and dimension brought about a synergistic effect for promoted electron transport and retarded charge recombination.

When the film thickness is taken into account, the electron transport time and electron lifetime become convertible into other meaningful parameters. For instance, diffusion coefficients (D_n) and effective diffusion length (L_n) can be used to make a fair comparison of intrinsic charge transfer and recombination dynamics of the systems under investigation. Certainly, the prerequisite is to maintain the film with similar thickness. Specifically, D_n and L_n can be estimated by the following expression: $D_n = d^2/(4\tau_d)$,[42] and $L_n = (D_n\tau_r)^{1/2}$,[43] respectively, where d is the film thickness. Figure 7b,c shows the D_n and L_n values of DSCCs based on the three TiO$_2$ photoanodes. The results reveal that the diffusion of electrons within multilayered TiO$_2$ cells is more efficient than that of TNP cells, implying that our engineered multilayered TiO$_2$ film provides a faster pathway for the electronic motion within the photoanodes. This conclusion might be understood from the morphological features of the TiO$_2$ architectures. In detail, our engineered multilayered TiO$_2$ film consists of hierarchical vertically aligned TiO$_2$ nanowires, hierarchical macroporous TiO$_2$ spheres, and hierarchical TiO$_2$ microspheres, which have all been proved to possess prominent electron transport characteristics. Also the subsequent hyperbranched modification may construct an interconnected network with a high degree of porosity and connect each TiO$_2$ layer tightly to form a remarkable very strong mechanical structure. These facts seem to promote electrolyte penetration and electron diffusion via multilayered photoanodes; however, it is generally believed that electron diffusion within the TNP film is interrupted by a series of trapping/detrapping processes because of numerous defects and grain boundaries existing in the nanocrystalline films.[44] Figure 7c showcases the L_n values of the three DSSCs. The results indicate a trend of L_n with an ambiguous order: AHTNW−MPT−HTS (~90 μm) > AHTNW−MPT−HTS−branches (~65 μm) > TNP (~45 μm). Normally, L_n values suggest whether an injected electron can transport to an external circuit prior to undergoing recombination,[45] and therefore a long diffusion length is preferred for an ideal TiO$_2$ film photoanode. Finally, charge collection efficiency (η_{cc}) is also a useful index to evaluate the performance of DSSCs based on different TiO$_2$ photoanodes. Typically, η_{cc} was calculated by gauging electron transport time and electron lifetime in a combined manner, using following the equation: $\eta_{cc} = 1 - (\tau_d/\tau_r)$.[46,47] As a consequence, η_{cc} values of 96% and 93% were demonstrated in the AHTNW−MPT−HTS based cell and AHTNW−MPT−HTS−branches based cell at 100 mW cm^{-2}, respectively, while the TNP cell only showed a limited η_{cc} of 85% (Figure 7d). It can be concluded that multilayered-based

cells have less surface traps, internal defects, and grain boundaries as compared with nanoparticle-based film, in which electrons trapped at the surface of such devices become fewer than for the TNP device, so that charge recombination is suppressed more effectively for the former than the latter, which is consistent with the aforementioned EIS, OCVD, and IMVS results.

4. CONCLUSIONS

To summarize, we have proposed, for the first time, a novel engineered multilayered stack photoanode on transparent FTO glass substrate, which embodied three different families of hyperbranched TiO_2 architectures. Notably, such a three-layer stack TiO_2 photoanode exhibited complementary and synergistic properties, in which a bottom layer made of densely packed hyperbranched TiO_2 nanowires can provide a direct electron transport pathway through 1D nanobuilding blocks and enable desirable electron extraction from nanowires to the FTO substrate; an intermediate layer consisting of branched submicrometer-sized macroporous TiO_2 spheres can guarantee effective light-trapping efficiency through the hollow-hole structure; and a third top layer composed of hyperbranched hierarchical TiO_2 microspheres can offer prominent light-scattering ability. Thus, this engineered integration made it possible to control the charge collection, charge transfer dynamics, and optical scattering simultaneously. It is worth noting that the hyperbranched modification was beneficial not only to further enhance the dye-loading capability, but also to strengthen the connection among the individual TiO_2 crystals through the interconnected TiO_2 short nanorod branches network. The device performance of DSSCs based on such a multistack photoanode is optimized to attain η = 11.01% (J_{sc} = 18.53 mA cm^{-2}, V_{oc} = 827 mV and FF = 0.72) at a film thickness of 34 μm, which is superior to that, η = 7.62%, of a reference conventional nanoparticles-type DSSC with a similar film thickness. Our work demonstrates the possibility to create engineered photoanodes with tailored textures and a high degree of integrated functionality, which are generally incompatible with each other, for instance, high charge-collection efficiency, fast electron transport, and pronounced light-harvesting efficiency. We believe that such a multilayered stack TiO_2 photoanode with hyperbranched TiO_2 architecture is a promising candidate for further promotion of ultimate light-to-electricity conversion efficiency of a DSSC or QDSSC device.

ASSOCIATED CONTENT

Ⓢ Supporting Information

Schematic sketch of film fabrication process; digital photograph of resultant TiO_2 film; XRD patterns of the multilayered TiO_2 photoanode and reference TiO_2 nanoparticles photoanode on FTO glass; SEM images of different TiO_2 photoanodes; diffused reflectance spectra of different TiO_2 photoanodes; summarized photovoltaic parameters of DSSC based on different TiO_2 photoanodes; Detailed simulative value of recombination resistance (R_2) and electron lifetime value (τ_r) from EIS spectra. This material is available free of charge via the Internet at http://pubs.acs.org.

AUTHOR INFORMATION

Corresponding Author
kuangdb@mail.sysu.edu.cn

Notes
The authors declare no competing financial interest.

ACKNOWLEDGMENTS

REFERENCES
(1) O'Regan, B.; Grätzel, M. *Nature* **1991**, *353*, 737.
(2) Bae, J.; Song, M. K.; Park, Y. J.; Kim, J. M.; Liu, M. L.; Wang, Z. L. *Angew. Chem., Int. Ed.* **2011**, *50*, 1683.
(3) Lin, Z. H.; Xie, Y. N.; Yang, Y.; Wang, S. H.; Zhu, G.; Wang, Z. L. *ACS Nano* **2013**, *7*, 4554.
(4) Yin, Z. Y.; Wang, Z.; Du, Y. P.; Qi, X. Y.; Huang, Y. Z.; Xue, C.; Zhang, H. *Adv. Mater.* **2012**, *24*, 5374.
(5) Yella, A.; Lee, H. W.; Tsao, H. N.; Yi, C. Y.; Chandiran, A. K.; Nazeeruddin, M. K.; Diau, E. W. G.; Yeh, C. Y.; Zakeeruddin, S. M.; Grätzel, M. *Science* **2011**, *334*, 629.
(6) Du, J.; Qi, J.; Wang, D.; Tang, Z. *Energy Environ. Sci.* **2012**, *5*, 6914.
(7) Ferber, J.; Luther, J. *Sol. Energy Mater. Sol. C* **1998**, *54*, 265.
(8) Lai, X. Y.; Halpert, J. E.; Wang, D. *Energy Environ. Sci.* **2012**, *5*, 9944.
(9) Grätzel, M. *Nature* **2001**, *414*, 338.
(10) Grätzel, M. *Acc. Chem. Res.* **2009**, *42*, 1788.
(11) Ye, M.; Zheng, D.; Lv, M.; Chen, C.; Lin, C.; Lin, Z. *Adv. Mater.* **2013**, *25*, 3039.
(12) Lv, M.; Zheng, D.; Ye, M.; Xiao, J.; Guo, W.; Lai, Y.; Sun, L.; Lin, C.; Zuo, J. *Energy Environ. Sci.* **2013**, *6*, 1615.
(13) Shiu, J. W.; Lan, C. M.; Chang, Y. C.; Wu, H. P.; Huang, W. K.; Diau, E. W. G. *ACS Nano* **2012**, *6*, 10862.
(14) Nazeeruddin, M. K.; De Angelis, F.; Fantacci, S.; Selloni, A.; Viscardi, G.; Liska, P.; Ito, S.; Bessho, T.; Grätzel, M. *J. Am. Chem. Soc.* **2005**, *127*, 16835.
(15) Wang, Q.; Ito, S.; Grätzel, M.; Fabregat-Santiago, F.; Mora-Sero, I.; Bisquert, J.; Bessho, T.; Imai, H. *J. Phys. Chem. B* **2006**, *110*, 25210.
(16) Zhang, Q. F.; Chou, T. R.; Russo, B.; Jenekhe, S. A.; Cao, G. Z. *Angew. Chem., Int. Ed.* **2008**, *47*, 2402−2406.
(17) Chou, T. P.; Zhang, Q. F.; Fryxell, G. E.; Cao, G. Z. *Adv. Mater.* **2007**, *19*, 2588.
(18) Chen, D. H.; Huang, F. Z.; Cheng, Y. B.; Caruso, R. A. *Adv. Mater.* **2009**, *21*, 2206.
(19) Sauvage, F.; Chen, D. H.; Comte, P.; Huang, F. Z.; Heiniger, L. P.; Cheng, Y. B.; Caruso, R. A.; Grätzel, M. *ACS Nano* **2010**, *4*, 4420.
(20) Koo, H. J.; Kim, Y. J.; Lee, Y. H.; Lee, W. I.; Kim, K.; Park, N. G. *Adv. Mater.* **2008**, *20*, 195.
(21) Liao, J. Y.; Lei, B. X.; Kuang, D. B.; Su, C. Y. *Energy Environ. Sci.* **2011**, *4*, 4079.
(22) Wu, D. P.; Zhu, F.; Li, J. M.; Dong, H.; Li, Q.; Jiang, K.; Xu, D. S. *J. Mater. Chem.* **2012**, *22*, 11665.
(23) Lei, B. X.; Luo, Q. P.; Yu, X. Y.; Wu, W. Q.; Su, C. Y.; Kuang, D. B. *Phys. Chem. Chem. Phys.* **2012**, *14*, 13175.
(24) Wang, Z. S.; Kawauchi, H.; Kashima, T.; Arakawa, H. *Coord. Chem. Rev.* **2004**, *248*, 1381.
(25) Hore, S.; Nitz, P.; Vetter, C.; Prahl, C.; Niggemann, M.; Kern, R. *Chem. Commun.* **2005**, *15*, 2011.
(26) Nazeeruddin, M. K.; Kay, A.; Rodicio, I.; Humphry-Baker, R.; Mueller, E.; Liska, P.; Vlachopoulos, N.; Grätzel, M. *J. Am. Chem. Soc.* **1993**, *115*, 6382.
(27) Ito, S.; Murakami, T. N.; Comte, P.; Liska, P.; Grätzel, C.; Nazeeruddin, M. K.; Grätzel, M. *Thin Solid Films* **2008**, *516*, 4613.
(28) Park, Y.-C.; Chang, Y.-J.; Kum, B.-G.; Kong, E.-H.; Son, J. Y.; Kwon, Y. S.; Park, T.; Jang, H. M. *J. Mater. Chem.* **2011**, *21*, 9582.

(29) De Marco, L.; Manca, M.; Giannuzzi, R.; Belviso, M. R.; Cozzoli, P. D.; Gigli, G. *Energy Environ. Sci.* **2013**, *6*, 1791.

(30) Chang, Y. J.; Kong, E. H.; Park, Y. C.; Jang, H. M. *J. Mater. Chem. A* **2013**, *1*, 9707.

(31) Wu, W. Q.; Xu, Y. F.; Su, C. Y.; Kuang, D. B. *Energy Environ. Sci.* **2014**, *7*, 644.

(32) Wu, H. P.; Lan, C. M.; Hu, J. Y.; Huang, W. K.; Shiu, J. W.; Lan, Z. J.; Tsai, C. M.; Su, C. H.; Diau, E. W. G. *J. Phys. Chem. Lett.* **2013**, *4*, 1570.

(33) Wu, W.-Q.; Lei, B.-X.; Rao, H.-S.; Xu, Y.-F.; Wang, Y.-F.; Su, C.-Y.; Kuang, D.-B. *Sci. Rep.* **2013**, *3*, 1352.

(34) Wu, W.-Q.; Rao, H.-S.; Xu, Y.-F.; Wang, Y.-F.; Su, C.-Y.; Kuang, D.-B. *Sci. Rep.* **2013**, *3*, 1892.

(35) Wu, W.-Q.; Liao, J.-Y.; Chen, H.-Y.; Yu, X.-Y.; Su, C.-Y.; Kuang, D.-B. *J. Mater. Chem.* **2012**, *22*, 18057.

(36) Fabregat-Santiago, F.; Bisquert, J.; Palomares, E.; Otero, L.; Kuang, D. B.; Zakeeruddin, S. M.; Grätzel, M. *J. Phys. Chem. C* **2007**, *111*, 6550.

(37) Kuang, D. B.; Klein, C.; Zhang, Z. P.; Ito, S.; Moser, J. E.; Zakeeruddin, S. M.; Grätzel, M. *Small* **2007**, *3*, 2094.

(38) Law, M.; Greene, L. E.; Johnson, J. C.; Saykally, R.; Yang, P. D. *Nat. Mater.* **2005**, *4*, 455.

(39) Wang, X. Y.; Liu, Y.; Zhou, X.; Li, B. J.; Wang, H.; Zhao, W. X.; Huang, H.; Liang, C. L.; Yu, X.; Liu, Z.; Shen, H. *J. Mater. Chem.* **2012**, *22*, 17531.

(40) Zaban, A.; Greenshtein, M.; Bisquert, J. *ChemPhysChem* **2003**, *4*, 859.

(41) Wang, H. X.; Nicholson, P. G.; Peter, L.; Zakeeruddin, S. M.; Grätzel, M. *J. Phys. Chem. C* **2010**, *114*, 14300.

(42) Dloczik, L.; Ileperuma, O.; Lauermann, I.; Peter, L. M.; Ponomarev, E. A.; Redmond, G.; Shaw, N. J.; Uhlendorf, I. *J. Phys. Chem. B* **1997**, *101*, 10281.

(43) Jennings, J. R.; Ghicov, A.; Peter, L. M.; Schmuki, P.; Walker, A. B. *J. Am. Chem. Soc.* **2008**, *130*, 13364.

(44) Wu, W.-Q.; Xu, Y.-F.; Rao, H.-S.; Su, C.-Y.; Kuang, D.-B. *Nanoscale* **2013**, *5*, 4362.

(45) Gonzalez-Vazquez, J. P.; Anta, J. A.; Bisquert, J. *J. Phys. Chem. C* **2010**, *114*, 8552.

(46) Zhu, K.; Vinzant, T. B.; Neale, N. R.; Frank, A. J. *Nano Lett.* **2007**, *7*, 3739.

(47) Oekermann, T.; Zhang, D.; Yoshida, T.; Minoura, H. *J. Phys. Chem. B* **2004**, *108*, 2227.